JGR Oceans

RESEARCH ARTICLE
10.1029/2019JC015307

Key Points:
- Intratidal salinity variation (ISV) and a strong lateral flow in a channel-shoal system were identified by an integrated tripod system
- Numerical simulation reveals that lateral flows were primarily driven by the salinity-induced pressure gradient force
- Lateral flows can be generated or enhanced by human interventions such as groyne fields

Correspondence to:
J. Ge,
jzge@sklec.ecnu.edu.cn

Citation:
Zhou, Z., Ge, J., Wang, Z. B., van Maren, D. S., Ma, J., & Ding, P. (2019). Study of lateral flow in a stratified tidal channel-shoal system: The importance of intratidal salinity variation. *Journal of Geophysical Research: Oceans*, *124*. https://doi.org/10.1029/2019JC015307

Received 23 MAY 2019
Accepted 24 AUG 2019
Accepted article online 29 AUG 2019

©2019. American Geophysical Union. All Rights Reserved.

Study of Lateral Flow in a Stratified Tidal Channel-Shoal System: The Importance of Intratidal Salinity Variation

Zaiyang Zhou[1,2], Jianzhong Ge[1,3], Zheng Bing Wang[2,4], D. S. van Maren[2,4], Jianfei Ma[1], and Pingxing Ding[1]

[1]State Key Laboratory of Estuarine and Coastal Research, East China Normal University, Shanghai, China, [2]Faculty of Civil Engineering and Geosciences, Delft University of Technology, Delft, The Netherlands, [3]Institute of Eco-Chongming (IEC), Shanghai, China, [4]Deltares, Delft, The Netherlands

Abstract Lateral flow significantly contributes to the near-bottom mass transport of salinity in a channel-shoal system. In this study, an integrated tripod system was deployed in the transition zone of a channel-shoal system of the Changjiang Estuary (CE), China, to observe the near-bottom physics with high temporal/spatial resolution, particularly focusing on the lateral-flow-induced mass transport. These in situ observations revealed a small-scale salinity fluctuation around low water slack during moderate and spring tidal conditions. A simultaneous strong lateral current was also observed, which was responsible for this small-scale fluctuation. A high-resolution unstructured-grid Finite-Volume Community Ocean Model has been applied for the CE to better understand the mechanism of this lateral flow and its impact on salinity transport. The model results indicate that a significant southward near-bed shoal-to-channel current is generated by the salinity-driven baroclinic pressure gradient. This lateral current affects the salinity transport pattern and the residual current in the cross-channel direction. Cross-channel residual current shows a two-layer structure in the vertical, especially in the intermediate tide when the lateral flow notably occurred. Both observation and model results indicate that near-bottom residual transport of water moved consistently southward (shoal to channel). Mechanisms for this intratidal salinity variation and its implications can be extended to other estuaries with similar channel-shoal features.

Plain Language Summary In channel-shoal systems, lateral processes sometimes can be of great significance, for example, influencing salinity and sediment transport, even some biogeochemical matters that influence the water environment. Salinity and sediment transport will have a further effect on navigability, ecology, and so on, for example, sediment deposition issues, which significantly decrease the shipping capacity. Consequently, knowing the accurate information about the flow field and finding a criterion for pronounced lateral processes are important to better understand hydrodynamics and sediment behaviors in channel-shoal systems. Here in this study, we conducted an in situ observation and used numerical simulation to detect and predict a strong lateral flow in the North Passage of the Changjiang Estuary. This shoal-to-channel lateral flow occurred around the end of ebb and caused an intratidal salinity variation at the observation site, close to the deep channel. Therefore, a link between pronounced lateral flows and typical salinity variation can be established. This link can also be found in other estuaries like Hudson River estuary. Findings presented here will help to easily distinguish pronounced lateral flows and better understand the effect of lateral flows.

1. Introduction

As transition zones between riverine and marine environments, estuaries experience a wide range of physical, chemical, and biological processes, for example, suspended material transport, chemical reaction of dissolved ions, and variation of biological productivity. These processes not only influence ecology but also have socioeconomic impacts because many large cities are located in the vicinity of estuaries (Woodroffe et al., 2006).

Salinity is a significant driver for sediment trapping, for example, sediment accumulation at the front of salt wedge where the convergence of fresh and saline water occurs (Postma, 1967). The upstream limit of salt intrusion is an indicator for location of estuary turbidity maximum (Dyer, 1986), the dynamics of which

in itself strongly influences the navigability. Moreover, salinity also has an effect on ecology, for example, its impact on temporal distribution of planktons (Dube et al., 2010).

The long-term, large-scale salt balance is primarily the result of landward transport by estuarine circulation and tidal dispersion (Bowen, 2003; Fischer, 1976) balancing seaward transport by riverine residual flow. These salt transport mechanisms depend on the longitudinal salinity gradient and (in combination with hydrodynamic mixing) give rise to vertical salinity gradients. Vertical salinity gradients may cause salinity stratification, which controls the intensity of momentum exchanges from the surface to the bottom (Simpson et al., 1990).

In addition to these longitudinal and vertical processes, lateral processes in estuaries also have effects on mass transport. Cross-channel (lateral) currents are relatively small (about 10% in magnitude) compared to the along-channel currents (Lerczak & Rockwell Geyer, 2004). However, their influences on dynamics of estuaries may be significant by generating considerable cross-channel gradients in salt, turbidity, and other constituents.

Lerczak and Rockwell Geyer (2004) set up a model for an idealized straight estuary. Their results suggest that lateral circulation is stronger during flood tides than ebb tides. This asymmetry is caused by the interaction between lateral circulation, stratification, and differential advection by along-channel tidal currents. The flood-ebb asymmetry of lateral flow patterns may lead to an asymmetric cross-sectional shape of a straight channel. However, in a channel that is already asymmetrically shaped, lateral flow will also be affected by bathymetric features, as well as hydraulic structures. Huijts et al. (2006) studied the mechanisms for lateral sediment entrapment using an idealized model. They examined mechanisms that could lead to the sediment accumulation, including Coriolis forcing and lateral density gradients. They found that because of the difference of along-channel flow velocity from bed to surface, the intensity of the Coriolis deflection varies from bed to surface. Therefore, vertical circulation in the lateral direction can be induced by the Coriolis deflection. Fugate et al. (2007) conducted an observation in upper Chesapeake Bay, USA, focusing on the impact of lateral dynamics on sediment transport. Using a lateral momentum balance, they observed that stronger cross-channel circulation by rotational effects (Coriolis and channel curvature) is larger during the ebb. A modeling study by Zhu et al. (2018) in a strongly anthropogenically impacted estuary (the Changjiang Estuary) suggests that lateral circulations are strong near the main navigation channel and peak close to slack tide conditions. This has great implications for siltation rates in the channel, in which more than 80 million m^3/year (by 2011) needs to be dredged annually (Wang et al., 2015). This fuels a great interest in the dynamics of lateral flows in general, but in the Changjiang Estuary (CE) in particular.

Cross-sectional flows influence the salinity, leading to an intratidal salinity variation (ISV). Many studies have identified the salinity's response to the longitudinal and vertical process (Bowen, 2003; Chen & de Swart, 2018; Dyer, 1986; Simpson et al., 1990). However, few observations directly relate salinity fluctuations to lateral flows. Yet, salinity variations may provide an indicator for lateral flows, which is much easier to measure than transverse flows themselves. The objective of this study is to detect evidence for lateral flow using a combination of flow velocity and salinity observations and quantitatively analyze and explain their driving mechanisms and effects. This paper is organized as follows. Section 2 introduces the study area, methods for observation and data analysis, and the numerical model. Section 3 presents the main results of observations and simulations, focusing on formation of ISV and the mechanism for the lateral flow. Section 4 gives discussion on momentum balance, stratification and mixing, effects of dikes and groynes, and the implication of ISV. Section 5 summarizes the main conclusions.

2. Study Site, Observation Methods, and Numerical Model

2.1. Study Site

Field observations were carried out in one of the four outlets of the CE (Figure 1). The discharge of the Changjiang River, measured at the Datong Gauging Station, is approximately 40,000 m^3/s in wet season and about 10,000 m^3/s in dry season. The mean and maximum tidal ranges are approximately 2.7 and 4.6 m, respectively, measured at Zhongjun Gauging Station.

The CE is characterized as a channel-shoal system with multiple outlets and shallow shoals. The South Channel (SC), North Passage (NP), and South Passage (SP) are the major tidal channels in the turbidity

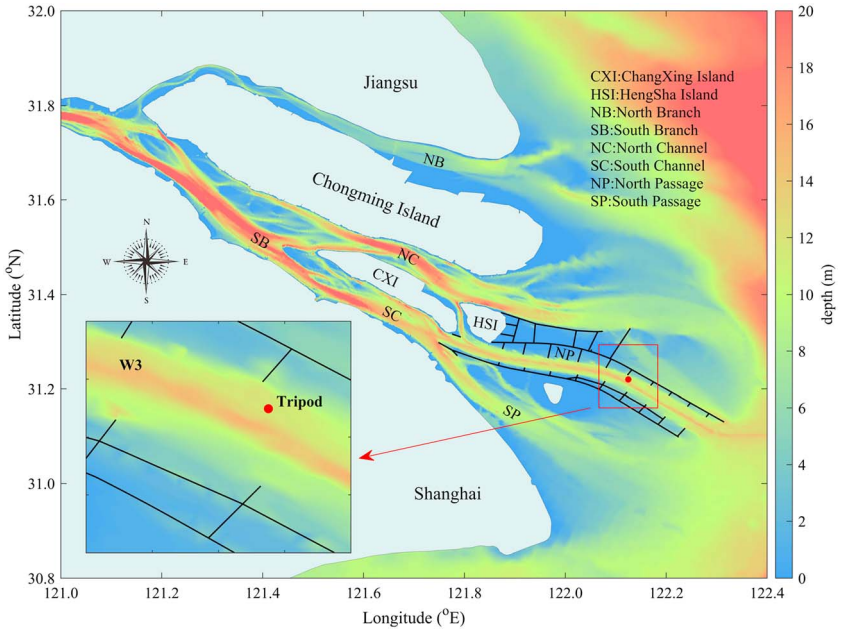

Figure 1. Bathymetry of the Changjiang Estuary and adjacent regions. The black lines in the river mouth indicate dikes and groynes around the North Passage. The red dot indicates the measuring site. W3 is the bending corner of the main channel.

maximum zone of the CE. The NP is deepened and protected, resulting in the so-called Deepwater Navigation Channel, aiming at improving the shipping capacity in and out of the CE. The protection works include two 50-km-long dikes parallel to the flow, to which 19 groynes perpendicular to the flow are attached (Figure 1).

The estuarine turbidity maximum of the CE is located in the NP, resulting in strong sedimentation rates (Ge et al., 2015, 2018; Liu et al., 2011). Many groynes have been buried since the construction of the Deepwater Navigation Channel. This has led to shallow shoals in the groyne region and a deeper main channel in the middle of the NP, forming a typical channel-shoal system. Cross-channel flows have been observed in the NP through observational and numerical studies (Liu et al., 2011; Zhu et al., 2018). The NP is also the main mixing front of freshwater and saline water, resulting in strong horizontal salinity gradient and vertical stratification (Ge et al., 2012, 2018; Wu et al., 2012).

2.2. Observation Methods

The middle section of the NP, located in the center of the turbidity maximum, was selected to conduct our observations (red rectangle in Figure 1). A tripod system was deployed on the north side of the main channel, an area with pronounced saltwater intrusion, and a strongly stratified water column (Ge et al., 2018). The observation site was in the middle of the shallow shoal and the main channel to observe lateral flows between the shoal and the deep channel.

The tripod system was designed to measure flow velocity and direction, salinity, suspended sediment concentration, and temperature near the bottom. To achieve this goal, the tripod integrated multiple instruments (Figure 2). An upward looking 600-kHz RDI Acoustic Doppler Current Profilers (ADCP-up) was mounted 1.2 m above the seabed (abbreviated as mab) with a resolution of 0.5 m for each cell. A downward looking 1,200-kHz RDI ADCP (ADCP-down) was placed 1.03 mab to measure velocities from 0.2 to 0.7 mab at high resolution (0.1 m) near the bed. Based on earlier observations (Liu et al., 2011), the ADCP with 1,200-kHz sensor frequency works well in the near-bottom area under typical high sediment concentration for this area. A Nortek Acoustic Doppler Vector was mounted at 0.4 mab to measure the near-bed current velocities at a sampling frequency of 16 Hz, which means that valid data were collected at the height of about 0.25 mab. The tripod system also included a Point Current Meter (ALEC, JFE ALEC CO., LTD, JAPAN) at 1.45 mab to obtain flow velocities in the blanking range of ADCP-up, a

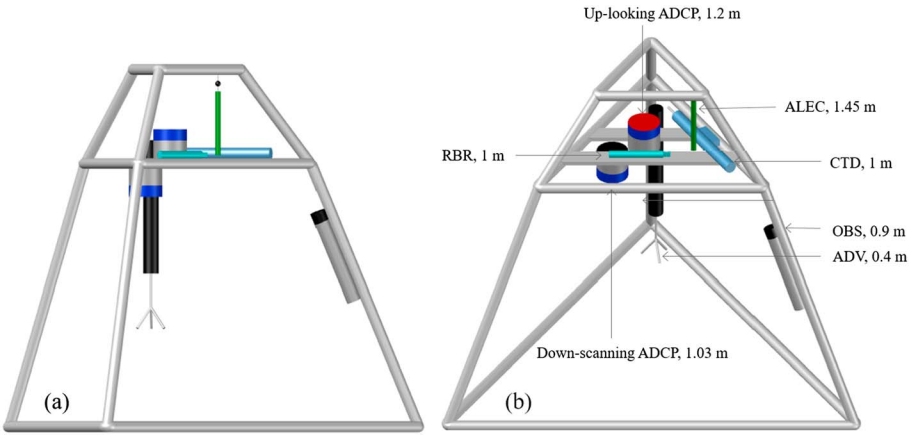

Figure 2. Side view and top view of the tripod system.

Tide/wave Logger (RBR, RBR Ltd., Canada) at 1.0 mab to record wave conditions, and a Conductivity, Temperature, and Pressure Recorder (CTD, Sea-Bird Electronics, Inc., USA) at 1.0 mab to record temperature and salinity continuously. An Optical Backscattering Sensor (OBS, D&A Instruments CO, type: 3A, USA) was also fixed to the side edge of the tripod. Detailed configurations of instruments installed on the tripod such as burst interval, sampling duration, and sampling frequency are listed in Table 1.

The tripod was deployed on 6 December 2016 (abbreviated as 12/06), in the dry season of the year. The observations lasted for about 12 days, and the tripod was recovered on 12/18, 2016. The 12 days covered a whole period from the neap tide to the spring tide. The neap tide was from 12/07 to 12/09, and the spring tide was on 12/14–12/16.

2.3. Numerical Model

To resolve the irregular geometries of the channel, shoals, and submerged/exposed dikes and groynes, a hydrodynamic numerical model based on the Finite-Volume Community Ocean Model has been applied for the CE (CE-FVCOM). FVCOM is a three-dimensional, unstructured-grid coastal ocean model. This model uses a triangle mesh in horizontal directions and a terrain-following sigma coordinate system with 20 uniform sigma layers in the vertical. Previous observations showed that the water column in the NP is occasionally strongly salinity stratified, and opposite flows form a two-layer flow structure in the vertical (Ge et al., 2013, 2018). As a mode split model, the adjustment between 3-D internal mode and 2-D external mode could be problematic for capturing this two-layer flow structure (Lai et al., 2010). Therefore, we use a semi-implicit scheme, which is capable of well simulating the two-layer structure flows.

The geographically unstructured mesh of FVCOM covers the whole CE and the inner shelf of the East China Sea, Hangzhou Bay, and Zhoushan Archipelago (Figure 3). Different from the original mesh configuration (Ge et al., 2012, 2013), the river boundary in this model is extended to ~ 600 km upstream Datong Gauging Station to better resolve the river estuary interaction (Figure 3a). It provides flexible resolution from the open

Table 1
Instruments Mounted on the Tripod and Their Sampling Configurations

Instrument deployed	Distance above bed (m)	Sampling interval (min)	Sampling configuration	Survey parameter
ADCP-up	1.2	/	120 s	Profile velocity
ADCP-down	1.03 (down)	/	120 s	Profile velocity
ADV	0.25	10	16 Hz (every first 70 s)	Near-bed velocity
RBR	1	10	4 Hz	Wave conditions
ALEC	1.45	2	0.2 Hz (every first 50 s)	Velocity
OBS	0.9	/	100 s	Salinity, temperature, turbidity, and pressure
CTD	1	/	120 s	Salinity, temperature, and pressure

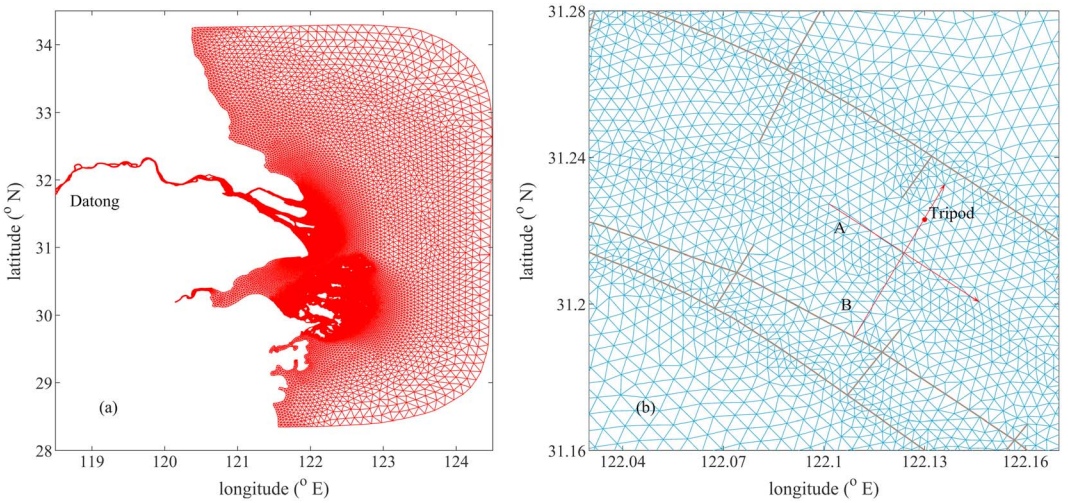

Figure 3. (a) Unstructured mesh for the Changjiang Estuary and adjacent regions. (b) An enlarged view within the NP. Section A, B is selected along- and cross-channel sections for analysis.

boundary in the inner shelf to channels and shoals at the river mouth. The horizontal resolution of this model is down to ~200 m in the channel (Figure 3b).

The model is forced by eight major astronomical tidal constituents specified at the open boundaries, including four diurnal tides (K_1, O_1, P_1, and Q_1) and four semidiurnal tides (M_2, S_2, N_2, and K_2). The data for the tidal constituent sources are from TPXO 8 (Egbert & Erofeeva, 2002). Daily river discharge of the CJ (data source: www.cjh.com.cn) is considered at the upstream boundary at Datong Gauging Station. The atmospheric forcing is the ERA-Interim data from the European Centre for Medium-Range Weather Forecasts with 0.125° spatial resolution and 3-hr temporal resolution. This model is discretized into 20 uniform terrain-following sigma layers, which provides sufficient vertical resolution for the bathymetry of 5–13 m in this channel-shoal system. The time step is set to 10 s with a spin-up time of 15 days. For the turbulence scheme, a Mellor and Yamada Level 2.5 turbulent closure scheme with Galperin modification is applied (Chen et al., 2003; Galperin et al., 1988; Mellor & Yamada, 1982). The horizontal and vertical Prandtl numbers defined as the ratio of turbulent eddy viscosity to the turbulent diffusivity (Chen et al., 2013) are 1.0 and 0.4, respectively.

3. Results

3.1. General Physics (Flow Velocity and Salinity)

The main data measured by various instruments of the tripod, including water levels, fixed-point velocity, and salinity, are shown in Figure 4. The whole observation period can be divided into three phases according to the tidal condition: Phase A from 12/07 to 12/11 (neap tidal conditions), Phase B from 12/11 to 12/14 (intermediate tidal conditions), and Phase C from 12/14 to 12/18 (spring tidal conditions).

The tidal range during neap tides was ~2 m and increased to ~4 m during spring tides (Figure 4a). The average bottom current velocity at 1.45 mab during neap tides was 44.5 cm/s, and almost double during spring tides, reaching 86.1 cm/s (Figures 4b and 4c). The maximum current velocity exceeded 150.0 cm/s during ebb tide. The mean flood duration during neap tides was 7.29 hr, whereas the mean ebb duration was 5.25 hr.

The cross-channel velocity component was irregular during neap tides (Figure 4c) with weak-amplitude fluctuation. The maximum cross-channel velocity during neap tides is ~25 cm/s (06:45 LST on 12/07). During intermediate and spring tidal conditions, the cross-channel velocity had a pronounced flow asymmetry. During intermediate tides, southward cross-channel flow occurred for 57% of time (with the remaining 43% northward flow), increasing to 68% of time during spring tides. Also, the average strength of southward flow was greater: 15.1 cm/s during intermediate tides and 17.0 cm/s during spring tides

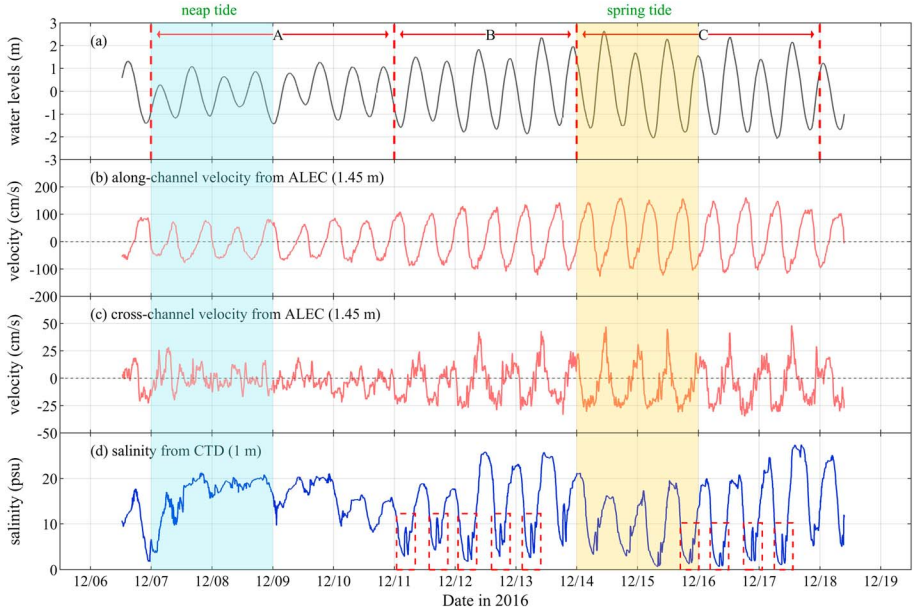

Figure 4. Time series of (a) water levels, (b) horizontal along-channel and (c) cross-channel velocity from ALEC, and (d) water salinity from CTD by the tripod. An orthogonal coordinate according to channel direction is used for velocity decomposition. For along-channel flow, the positive value indicates direction of about 120° from the north; for cross-channel flow, the positive value indicates direction of about 30° from the north.

(11.6 and 15.6 cm/s for northward flow for the respective tidal conditions). Consequently, there is a pronounced (shoal-to-channel) cross-channel velocity component, both in magnitude and duration, resulting from lateral flows.

The bottom salinity remained above ~20.0 PSU for several days with only small oscillations during neap tides. This indicates that the area remains in the range of the salt wedge during neap tides, as observed earlier by Ge et al. (2018). During intermediate and spring tidal conditions, an oscillating salinity pattern can be observed, with values ranging from nearly 0 PSU around the low water slack to 30 PSU around the high water slack (Figure 4d). In addition, from 12/11 to 12/18 (phases B and C), a series of significant oscillations lasting for about 2 hr with magnitude of about 5 PSU occurred in each trough of salinity curve (Figure 4d). We refer to these oscillations as ISV and will be elaborated on in more detail in the next section.

3.2. Identification of ISV

The ISVs were highly consistent with the tidal phase, always occurring during low water slack (marked by red rectangles in Figure 4d). During an ISV, the salinity first increases for about 20 min and then drops for about 51 min (averaged value of 5 ISVs during intermediate tides). Although the ISVs were identified during intermediate and spring tidal conditions, the amplitude was larger and the duration was longer during intermediate tides. The ISVs disappeared shortly before saline flood currents entered the NP close to the observation area. During this period, the upper water column was dominated by ebb currents, while the bottom area was dominated by flood currents (Figures 5e and 5h). This typical two-layer current structure occurred during low water slack (between ebb and flood), with weak currents in the whole water column. Importantly, during a period when ISVs occurred (green dashed lines in Figures 5f and 5i), the flow direction was ~210° from the north (Figures 5e and 5h).

The observation indicates that the formation of ISV is related to lateral flows. However, this measurement only demonstrates the ISV in a local perspective. It is unable to resolve the horizontal and vertical propagation of the water and salinity mass under the effect of the lateral flow. Therefore, the mechanism for the formation of ISV needs to be examined with a numerical model, allowing a more detailed quantitative analysis of the lateral flows.

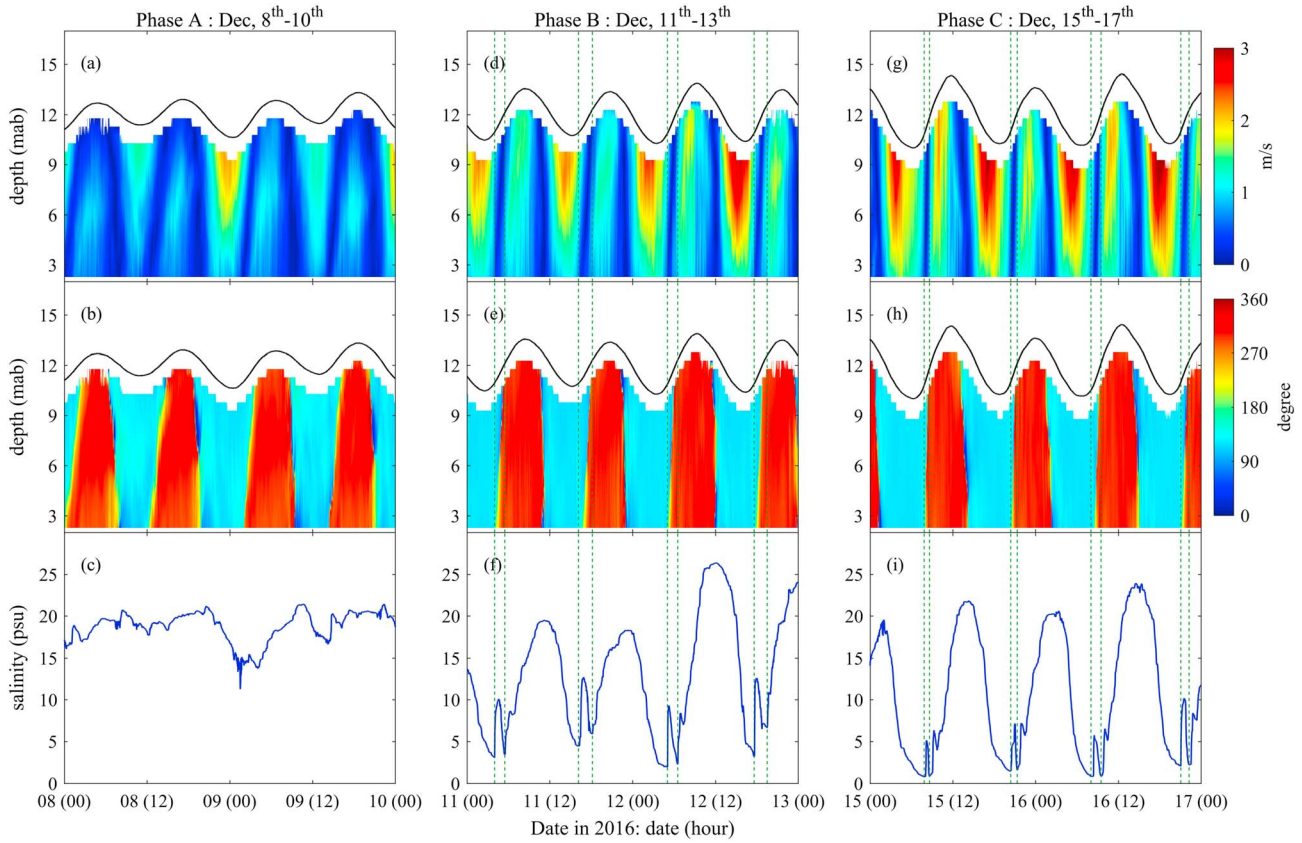

Figure 5. Time series of vertical profiles of flow velocity (row 1), flow direction (row 2), near-bed salinity (row3) during neap tides (left column), and intermediate tides (middle column) and spring tides (right column). The green dashed lines mark the occurrence of ISVs.

The applied model (CE-FVCOM) has been fully validated against hydrodynamics, tide, and salinity in previous studies (Ge et al., 2014, 2015; Guo et al., 2018). For example, averaged M_2 tidal amplitude error $((H_{\text{model}} - H_{\text{observation}})/H_{\text{observation}})$ at 32 gauge stations in the CE and adjacent coastal areas is 4% (Table 3 in Ge et al., 2014). In this study, model results are only compared to our tripod data for further validation. A comparison of near-bed flow velocity, direction, and salinity (shown in Figure 6) shows that the model captures the magnitude and direction of the upward looking ADCP (data of the first cell, 2 mab), and the variation of salinity collected by CTD. The overall root-mean-square errors for velocity magnitude, velocity direction, and salinity are 0.19 m/s, 15.1°, and 2.6 PSU, respectively. Even more, the ISVs occurring during intermediate and spring tidal conditions are also well resolved by the model (an example is marked with green dashed box in Figure 6c). The magnitude of modeled ISVs is slightly smaller than that of observed ISVs. The semi-implicit scheme used in this study is capable of better simulating the two-layer current structure. It may underestimate the water flux exchange along the groynes compared to the explicit scheme, which implements a generalized dike-groyne module, particularly during the flood tide period (Ge et al., 2012). This may cause an underestimation of salinity in the groyne-sheltered area and the smaller magnitude of ISVs as well. Since the model predicts the occurrence and correct timing of the ISVs, the model can be used to further explore formation mechanisms in more detail.

3.3. Formation and Breakdown of the ISV

To understand the formation and breakdown of ISV, a typical ISV during neap-to-spring transition tides is selected (marked by a green dashed rectangle in Figure 6c) for analysis with the numerical model. At the end of ebb, the salinity in the channel (including the observation site, Figure 7a) was low, while the shoals are more saline. The higher salinity on the shoals generates a near-bed salinity-driven density current peaking at 0.5 m/s (Figures 8e and 8f). The transport of more saline water from the shoals toward the channel leads to an increase in near-bed salinity (Figures 7a–7c), giving rise to the formation of ISV.

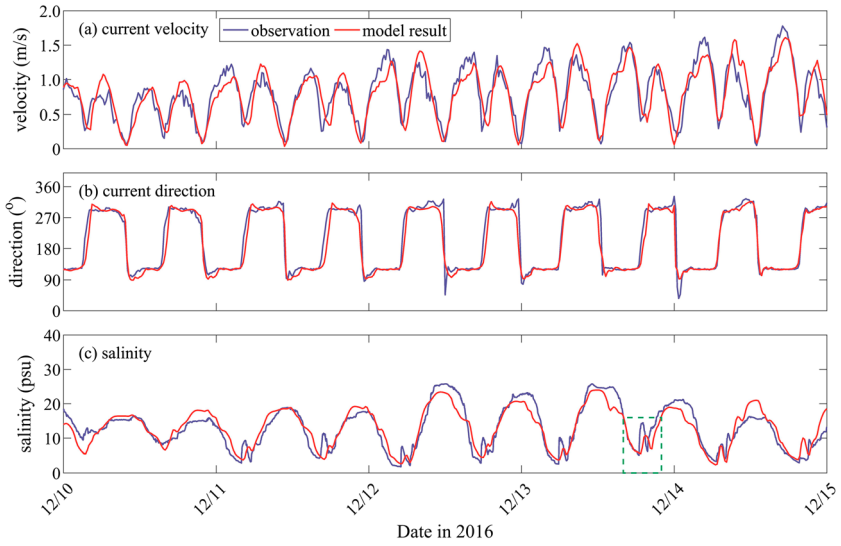

Figure 6. Model-data comparison between observed (blue) and simulated (red) results for near-bed tide current velocity (a), current direction (b), and salinity (c) at the observation site. The green dashed rectangle in (c) shows a typical intratidal salinity variation (ISV), and this ISV will be discussed in details in the following sections.

The amount of saline water stored over the shoals is limited, however. The high-salinity patch flows 1.5 km into the channel (Figures 8f and 8g) after which it dilutes or is advected up-estuary (Figures 8g–8i). During the period of maximum cross-channel flow (Figure 8e), the near-surface ebb currents are close to 1 m/s (Figure 9e). Such a large velocity gives rise to mixing, which is illustrated with the local salinity distribution. Near the observation point, the near-surface salinity increases (Figures 9f–9h) when the near-bed salinity decreases (Figures 8f–8h and 9f–9h). The salinity rapidly rises after flow reversal when the saline flood propagates into the channel (Figures 9i, 7e, and 7f).

Averaged over the tide, the lateral flows discussed above contribute to a tide-averaged cross-channel residual current (Figure 10). The variation of this tidally averaged cross current over the spring-neap tidal cycle can be evaluated with the upward looking ADCP observations. During the late neap tide and the intermediate tide when pronounced ISV was detected, the cross-channel residual current showed a clear vertical variability (Figures 10a and 10b). For the majority of time, the tidally averaged cross-channel component near the bed is directed toward the channel, whereas it is directed toward the shoals near the water surface.

4. Discussion

4.1. Mechanism for the Lateral Flow: Momentum Balance Analysis

Interpretation of the data and numerical model results suggests that the density-induced gradient resulting from the salinity difference between the channel and the shoal is the driving force for the lateral flow. We will further quantify this hypothesis using a momentum balance analysis.

We define the along-channel direction as the x axis (the positive value indicates a direction of 120° from the north) and the cross-channel direction as the y axis (the positive value indicates a direction of 30° from the north, away from the main channel), over which the governing equations for horizontal motions are given as follows:

$$\underbrace{\frac{\partial u}{\partial t}}_{A}+\underbrace{u\frac{\partial u}{\partial x}+v\frac{\partial u}{\partial y}+w\frac{\partial u}{\partial z}}_{B}\underbrace{-fv}_{C}=\underbrace{-\frac{1}{\rho}\frac{\partial(P_H+P_a)}{\partial x}}_{D}+\underbrace{\frac{\partial}{\partial z}\left(K_m\frac{\partial u}{\partial z}\right)}_{E}+\underbrace{F_x}_{F} \tag{1}$$

$$\underbrace{\frac{\partial v}{\partial t}}_{A}+\underbrace{u\frac{\partial v}{\partial x}+v\frac{\partial v}{\partial y}+w\frac{\partial v}{\partial z}}_{B}\underbrace{+fu}_{C}=\underbrace{-\frac{1}{\rho}\frac{\partial(P_H+P_a)}{\partial y}}_{D}+\underbrace{\frac{\partial}{\partial z}\left(K_m\frac{\partial v}{\partial z}\right)}_{E}+\underbrace{F_y}_{F} \tag{2}$$

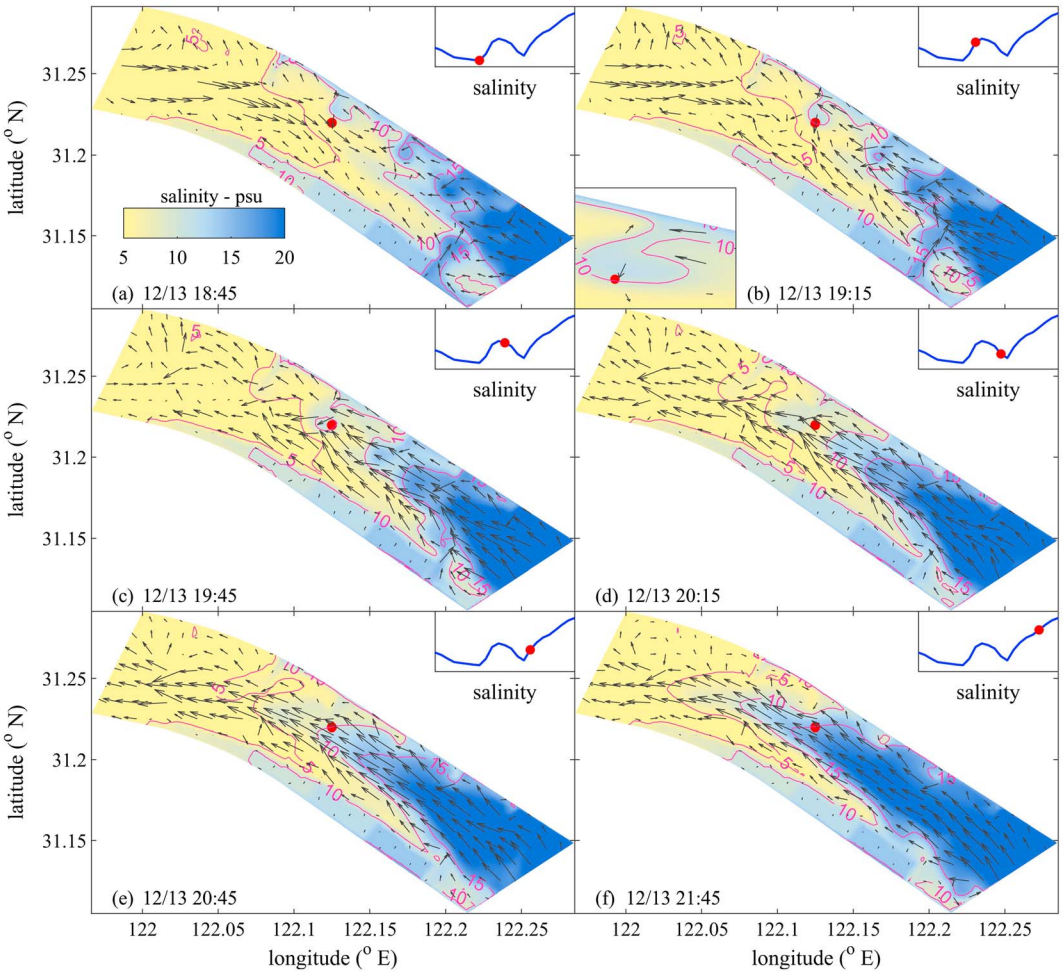

Figure 7. Spatial distributions of near-bed salinity and flow velocity at selected times (model result). The red dot indicates the observation site. The top right inset shows the process of ISV, and the red dot shows salinity of the site during this typical ISV period.

where x, y, and z are the horizontal and vertical axes of the Cartesian coordinate; u, v, and w are the x, y, and z component velocities, respectively; ρ is density; P_H is hydrostatic pressure; P_a is the air pressure at sea surface; f is the Coriolis parameter; and K_m is vertical eddy viscosity coefficient. Here, F_x and F_y represent the horizontal momentum diffusion terms in the along- and cross-channel directions, respectively.

The air pressure is omitted due to its weak contribution to the local hydrodynamics in the channel-shoal system. The hydrostatic pressure P_H satisfies

$$\frac{\partial P_H}{\partial z} = -\rho g \Rightarrow P_H = \rho_0 g\zeta + g\int_z^0 \rho dz \tag{3}$$

where g is the gravitational acceleration.

In equations (1) and (2), $A - F$ denote the local acceleration, advection, Coriolis force, pressure gradient, and vertical and horizontal momentum diffusion terms, respectively. The pressure gradient force term includes the barotropic (surface elevation) pressure gradient force and baroclinic (density) pressure gradient force as described in equation (3).

Figure 11 shows the vertical distribution of momentum terms of the Coriolis force and baroclinic pressure gradient (BPG) along the selected section B at selected times at before (18:30), right on the crest of (19:30) and after (20:15) a significant ISV on 12/13. The BPG was ~−3 * 10^{-4} m/s^2 at 18:30 LST 12/13 in the shoal

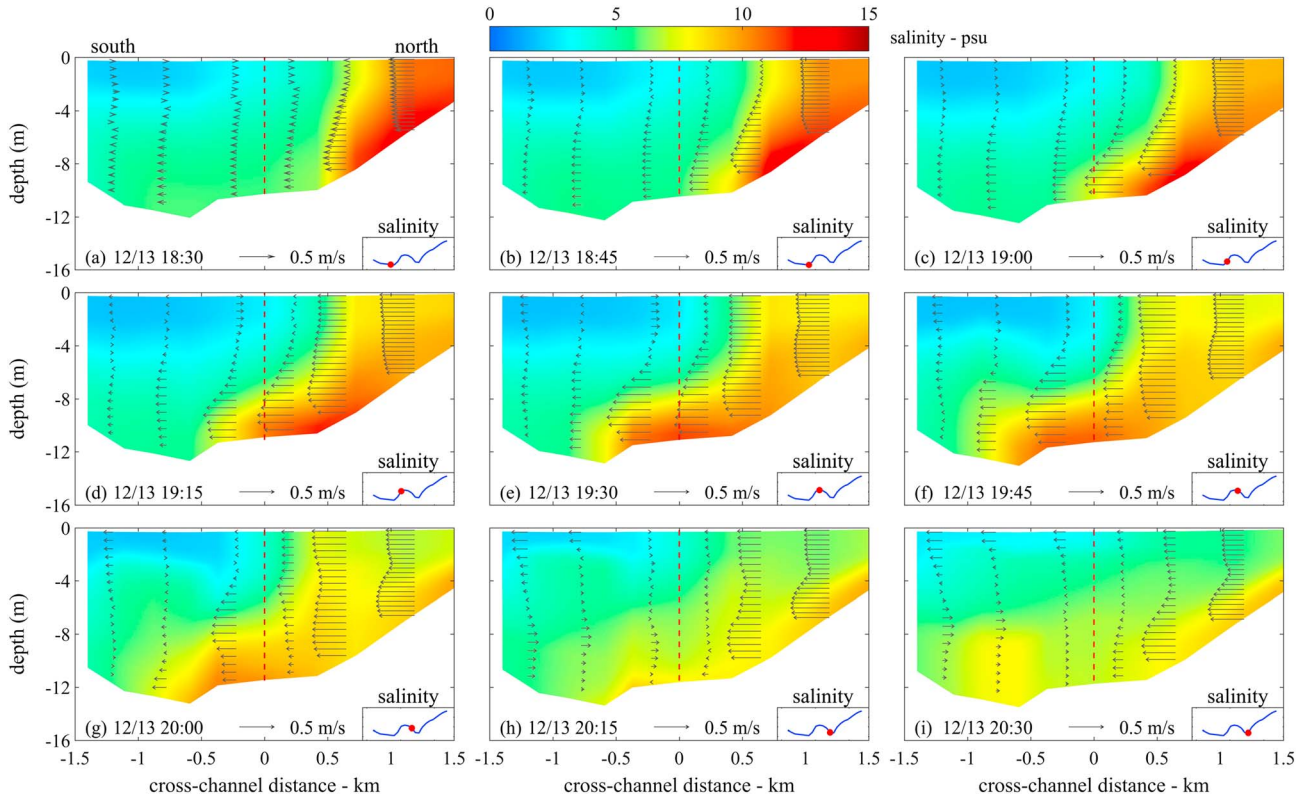

Figure 8. Vertical distribution of salinity and cross-channel flow velocity (arrows) at selected times (a typical ISV period). Red dashed line indicates the projection position of the observation site in a south-north cross-channel section (section B in Figure 3b). The bottom right insets show the process of ISV, and the red dot shows salinity of the site during this typical ISV period.

area (Figure 11d). The Coriolis force was ~−4 * 10^{-5} m/s^2, 1 order of magnitude smaller than the BPG since tidal currents are weak during low water slack (Figure 11a). The BPG and Coriolis force jointly drove the flow southward (from the north shoal to the main channel), generating the lateral current. In this stage, the BPG was the major contributor among all dynamical forces. At 19:30 LST 12/13, the BPG continued to drive the southward lateral flow, counteracted by the Coriolis force because near bottom this Coriolis force was in the northward direction (Figure. 11b). Similarly, the Coriolis force was 1 order of magnitude smaller than the BPG. Therefore, this hindrance effect could not substantially inhibit the development of the lateral flow. At the end of the ISV period when flood currents flowed into the channel, and the Coriolis force was in the northward direction in the whole section (Figure 11c), the BPG in the deep channel increased and had a northward component because of the movement of saline water (Figure 11f). Later, BPG in the deep channel would continue to increase due to seawater intrusion.

The momentum term due to flow curvature is also estimated. Equations (1) and (2) are written in Cartesian coordinate, which do not contain separate momentum term induced by channel curvature. The momentum equation can be written in curvilinear coordinate as follows (Chant, 2010):

$$\frac{\partial u_n}{\partial t} + u_s \frac{\partial u_n}{\partial s} - \frac{{u_s}^2}{R} + f u_s + g\frac{\partial \eta}{\partial n} - \frac{\partial \tau}{\partial z} = 0 \tag{4}$$

where s, n, and z represent main flow and lateral and vertical directions; u_s, u_n are velocity components in s, n directions; R is the radius of curvature; f is the Coriolis parameter; η is water level; and τ is stress. In equation (4), $\frac{{u_s}^2}{R}$ is momentum term of channel curvature, which is also named centrifugal acceleration. The longitude and latitude information of the north dike is transferred into a Cartesian coordinate, using a map-projection method. Then the new position of the north dike in the Cartesian coordinate is fitted with a quadratic curve to calculate R. For cross-channel section B (Figure 3b), which passes the observation site,

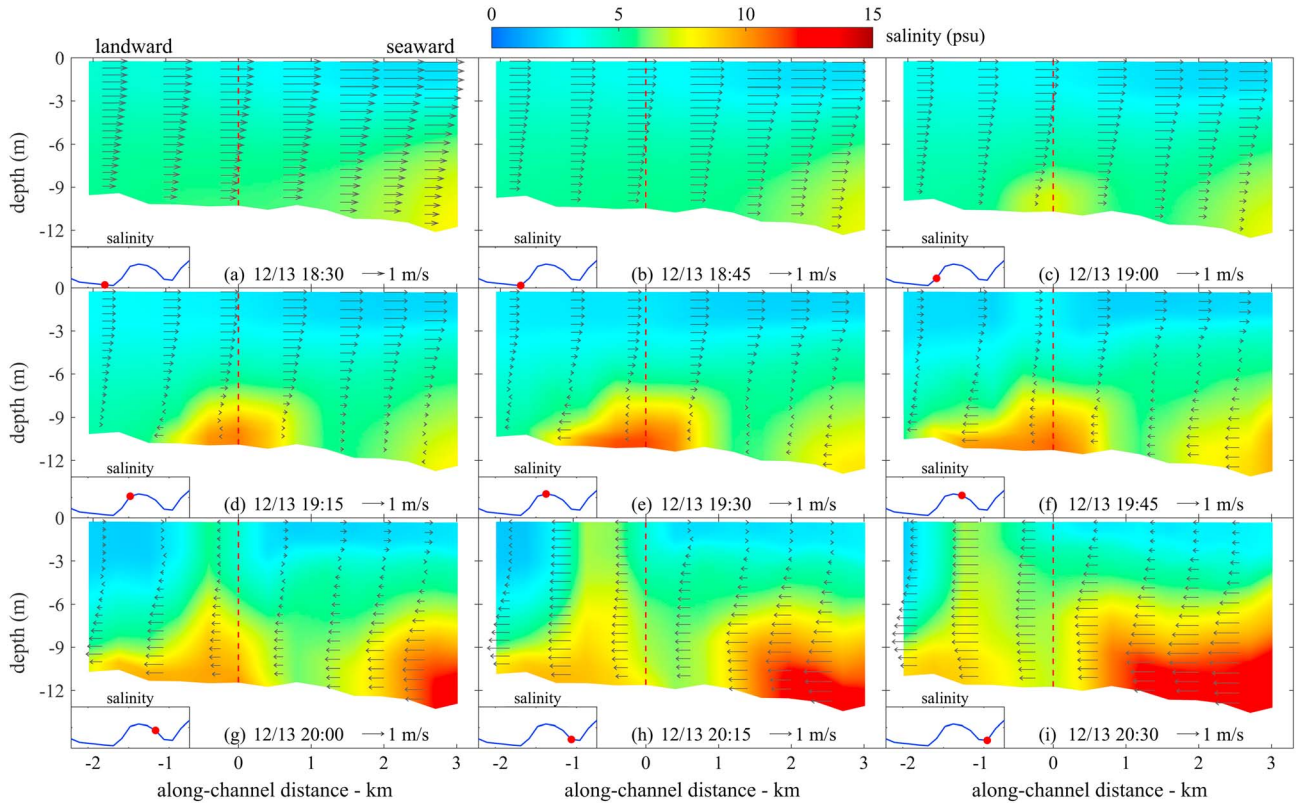

Figure 9. Vertical distribution of salinity and along-channel flow velocity (arrows) at selected times (a typical ISV period). Red dashed line indicates the projection position of the observation site in a west-east along-channel section (section A in Figure 3b). The bottom left inset shows the process of ISV, and the red dot shows salinity of the site during this typical ISV period.

$R \approx 49.7$ km, maximum magnitude of u_s was about 1.9 m/s (Figure 5b); thus, maximum value of $\frac{u_s^2}{R}$ was about $7.3 * 10^{-5}$ m/s^2. At the beginning of ISV (18:30 LST 12/13), u_s was about 0.2 m/s, and the effect of channel curvature was several orders of magnitude smaller than that of the BPG. Therefore, the BPG caused by the horizontal salinity gradient was the main driving force for the formation of the lateral flow.

Closer to the channel bend (Figure 1), $R \approx 28$ km, and here curvature effects could be larger. During the ebb tide, the maximum value of $\frac{u_s^2}{R}$ is about $1.3 * 10^{-4}$ m/s^2, toward the outside of the channel, while the Coriolis force is about $-1.1 * 10^{-4}$ m/s^2. These two forces were close, and the joint effect is small. However, during the flood tide, maximum centrifugal acceleration is about $1.0 * 10^{-4}$ m/s^2, while the Coriolis force is about $1.3 * 10^{-4}$ m/s^2. The combined effect of channel curvature and Coriolis force (about $2.3 * 10^{-4}$ m/s^2 in total) is comparable to that of the BPG, which generates the lateral flow. In the other word, this combined effect could also lead to an opposite lateral flow during flood tide period close to the river bend.

Because u_s in the channel curvature term is squared, this term always has the same sign within a whole tidal cycle. It may therefore strengthen or weaken the Coriolis term in different stages of a tidal cycle, giving rise to tidal asymmetry in lateral flows during flood and ebb tide (Chant, 2010). In many cases, lateral flow or lateral circulation could be dominated by the centrifugal acceleration for a period in a tidal cycle (Kim & Voulgaris, 2008; Lacy & Sherwood, 2004; Nidzieko et al., 2009) as the radius of curvature R is much smaller than that in our study. Although R is relatively large and the curvature-induced term appears to be less important than other terms, variation of R leads to different lateral circulation patterns in different cross-channel sections of the NP. In this study, the maximum joint effect of Coriolis term and centrifugal term is still smaller than the BPG when ISV was generated, indicating the significance of the trapped saline patch in the shallow shoal and the intensity of this lateral flow.

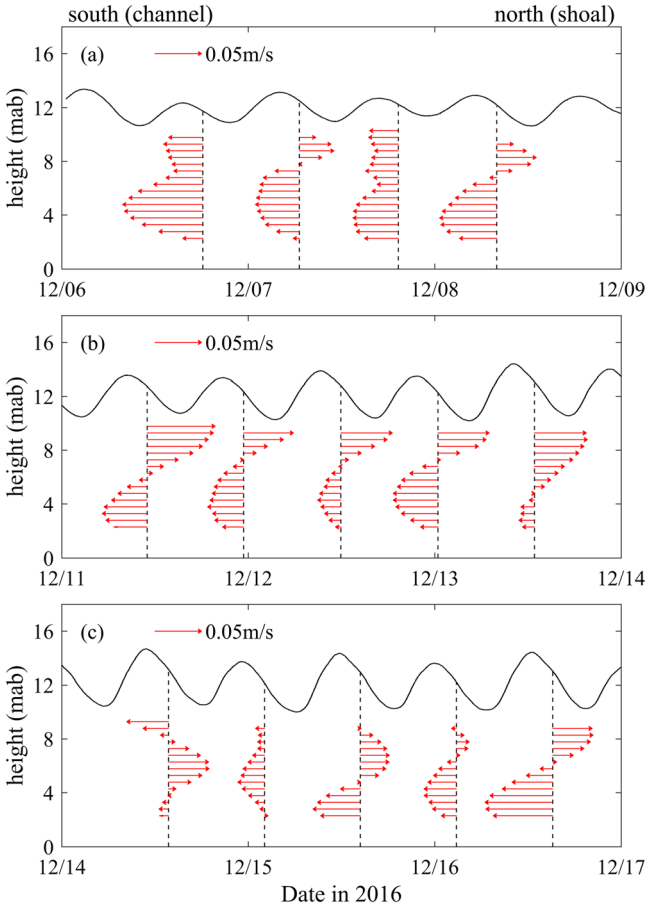

Figure 10. Tidally averaged cross-channel residual current calculated from ADCP results in (a) neap tide, (b) intermediate tide, and (c) spring tide at the observation site.

4.2. Stratification and Mixing

Differential advection of the water mass leading to ISV greatly influences stratification and mixing process in the channel-shoal system. During the ISV period, the cross-channel and along-channel salinity distribution and velocity showed a pronounced vertical variability (Figures 8 and 9). To what extent feedback mechanisms exist between salinity-induced stratification and the flow is further investigated with the gradient Richardson number (R_i):

$$R_i = -\frac{g}{\rho_w}\frac{\partial\rho/\partial z}{\left[\left(\frac{\partial u}{\partial z}\right)^2+\left(\frac{\partial v}{\partial z}\right)^2\right]} \tag{5}$$

where ρ_w is water density, $\partial\rho/\partial z$ is density gradient, and u,v are velocity components in x, y directions. The water column stratifies when R_i exceeds 0.25. Therefore, $\log_{10}(Ri/0.25)$ is used as an index for the degree of stratification (Figure 12, with positive values indicating stratifying conditions). The density of water did not always increase from the surface to the bottom, resulting in negative values of R_i, which give rise to the blank areas in Figure 12 when taken as a logarithm. As explained earlier, the saline water remaining in the shallow areas flowed downslope at the end of the ebb due to horizontal density differences, giving rise to the ISV. As a result of this density current, the near-bed channel gradually became more stratified (Figure 12c) by differential advection of salinity. During the peak of the ISV (Figure 12c), the larger part of the water column was salinity-stratified. However, the layer very close to the bed had a weak stratification (Figure 12c). This is because of the large gradient of velocity in the near-bed area due to the friction (Figure 8e).

The gradient Richardson number (R_i) indicates the stratification at a specific height in the whole vertical column, while the bulk Richardson number (R_{ib}) provides information of the whole water column (bottom to surface). R_{ib} can be calculated as (Hoitink et al., 2011; Lewis, 1997)

$$R_{ib} = \frac{gD\Delta\rho}{\overline{\rho_w}\left|\overrightarrow{u_s}^2\right|} \tag{6}$$

where D is the water depth, $\Delta\rho$ is the density difference between surface and bottom, $\overline{\rho_w}$ is the averaged density of the water column, and $\overrightarrow{u_s}$ is the horizontal velocity at the surface. The gradient Richardson number of different layers and the bulk Richardson number are shown in Figure 13. Turbulent kinetic energy (TKE) per unit mass is also used for further interpretation of vertical mixing. TKE can be calculated using the high-frequency velocity data collected by ADV as

$$TKE = \frac{1}{2}\left(\overline{u'^2}+\overline{v'^2}+\overline{w'^2}\right) \tag{7}$$

where u', v', and w' are velocity fluctuations of the streamwise, lateral, and vertical components and the overbar denotes time-averaging values.

Green, blue, and red dashed lines in Figure 13 indicate the start, peak (salinity maximum), and end of the ISV, respectively. Note that Figure 13a is based on model results, while Figures 13b and 13c are based on results of the tripod observation. Therefore, a small time lag of ISV process between these two methods can be found in Figure 13 (vertical dashed lines are different in three subgraphs). Shortly before the start of the ISV (green dashed lines), the near-bottom R_i and R_{ib} were below 0.25 (Figure 13a), indicating well-mixed condition. Both the time variation in near-bed salinity ($dsal/dt$, Figure 13c) and vertical salinity variation (Figure 8a) were small. All information therefore suggests a steady, well-mixed water column near the

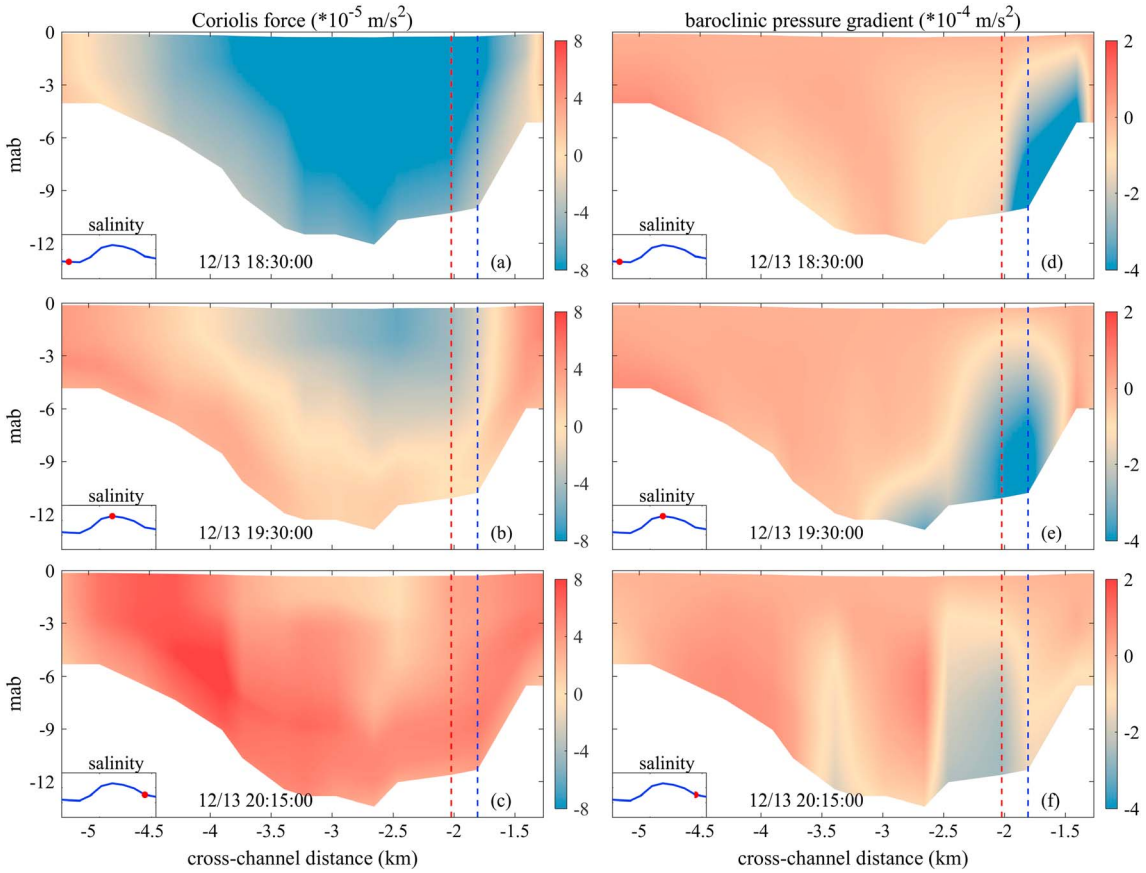

Figure 11. Vertical distributions of Coriolis force (left column) and baroclinic pressure gradient (right column) along the selected cross-channel section B in the ISV period. The red dashed line indicates the location of the observation site, and the blue dashed line shows an adjacent location north to the site. The bottom left inset shows the process of ISV in salinity, and the red dot shows salinity of the site during this typical ISV period.

end of the ebb. During the first stage of the ISV (between green and blue dashed lines), the salinity and R_{ib} increased rapidly (Figure 13). R_i at 1.5 mab showed a different variation from R_i at 0.5 and 1.0 mab. At 1.5 mab, there was a pronounced stratification as it was close to the interface between water in the salinity patch and ambient water. During the decreasing stage of the ISV (between blue and red lines), the whole water column (as indicated with the bulk Richardson number) remained stably stratified ($R_{ib} > 0.25$). The near-bed gradient Richardson numbers suggest a nonstratified water column, but this was because the halocline was located higher up in the water column. The observation that the water column was stratified during the decline of the ISV suggests that longitudinal advection (and not mixing) was the main mechanism responsible for the salinity decrease. Well-mixed conditions ($R_{ib} < 0.25$) reestablished halfway the flood, during periods of high TKE.

4.3. Effects of Dikes and Groynes

The investigated tidal channel was surrounded toward both the south and north with dikes and overflowing groynes (Figure 1). Although the main parts of the groynes from the tip are submerged by sediment deposition, the remaining parts near dikes are still exposed during low tide, which shapes the groyne-sheltered area as a semienclosed region. The groynes create nearly stagnant water masses and therefore strengthen differential advection of salt water. As a result, these groynes may greatly contribute to the transverse flows (and therefore ISV).

The effect of groynes is quantified by rerunning the model with one groyne (nearest to the observation site) removed. As a result, the ISV is no longer predicted at the observation site (Figure 14a). The bottom salinity distribution clearly shows that no high-salinity water is trapped in the north shoal without the groyne (Figure 14c). This is also clear in vertical salinity distribution in the cross-channel section, and

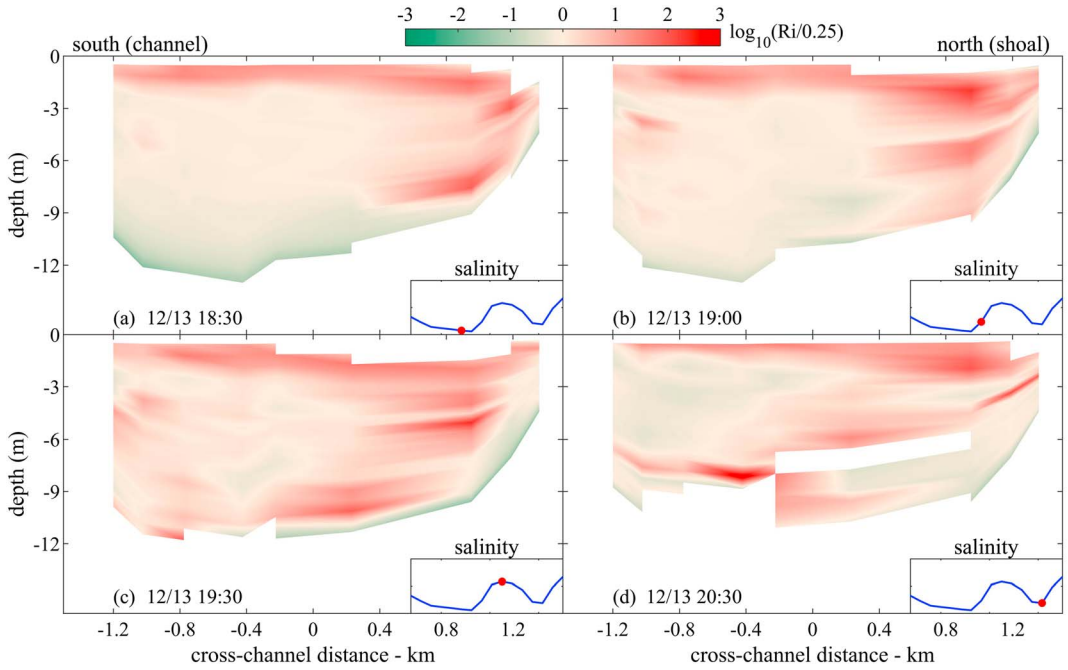

Figure 12. Distribution of $\log_{10}(Ri/0.25)$ in cross-channel section B (a) before the ISV, (b) in the increasing stage of ISV, (c) at the peak of ISV,and (d) at the end of the ISV. The zero position in x axis indicates the position of the observation site in the section. The bottom right inset shows variation of salinity and the time stamp salinity at the site.

cross-channel velocity is much smaller than the original case (Figure 14e). For downstream areas where groynes are still present, salinity is still influenced by the groynes (Figure 14c).

The numerical model results suggest that the groyne fields north of our observation site contribute much stronger to the generation of ISV's than their southern counterparts. Due to the retention effect all along the northern groynes, lateral flows developed, and the salinity varied over the tidal cycle (Figure 7). This was not true, however, for the southern groynes. The southern groynes were connected by an additional

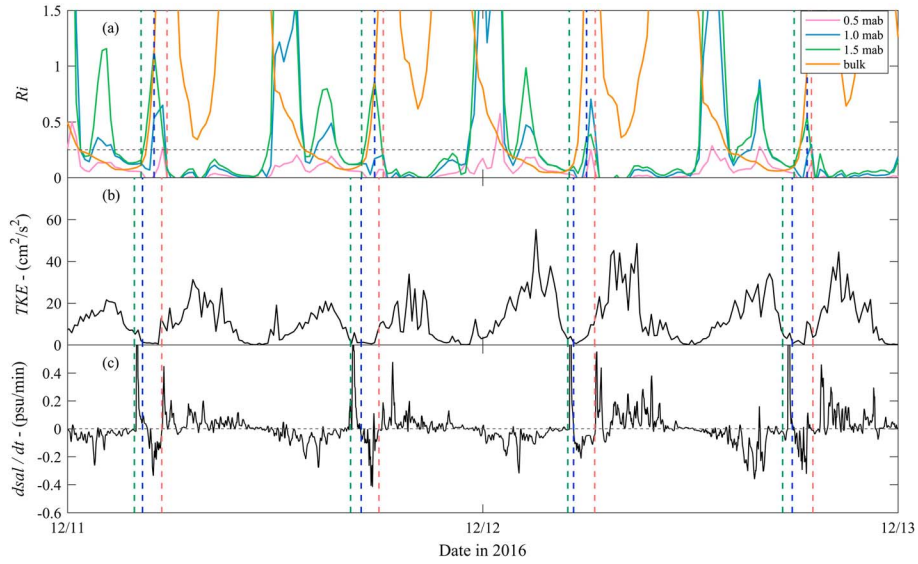

Figure 13. Time series of (a) gradient Richardson number at 0.5 mab (pink), 1.0 mab (blue), and 1.5 mab (green) and bulk Richardson number (orange), (b) turbulent kinetic energy (TKE) at the observation site, and (c) rate of salinity change in time. Green and blue dashed lines indicate the increasing stage in the ISV; blue and red dashed lines indicate the decreasing stage in the ISV.

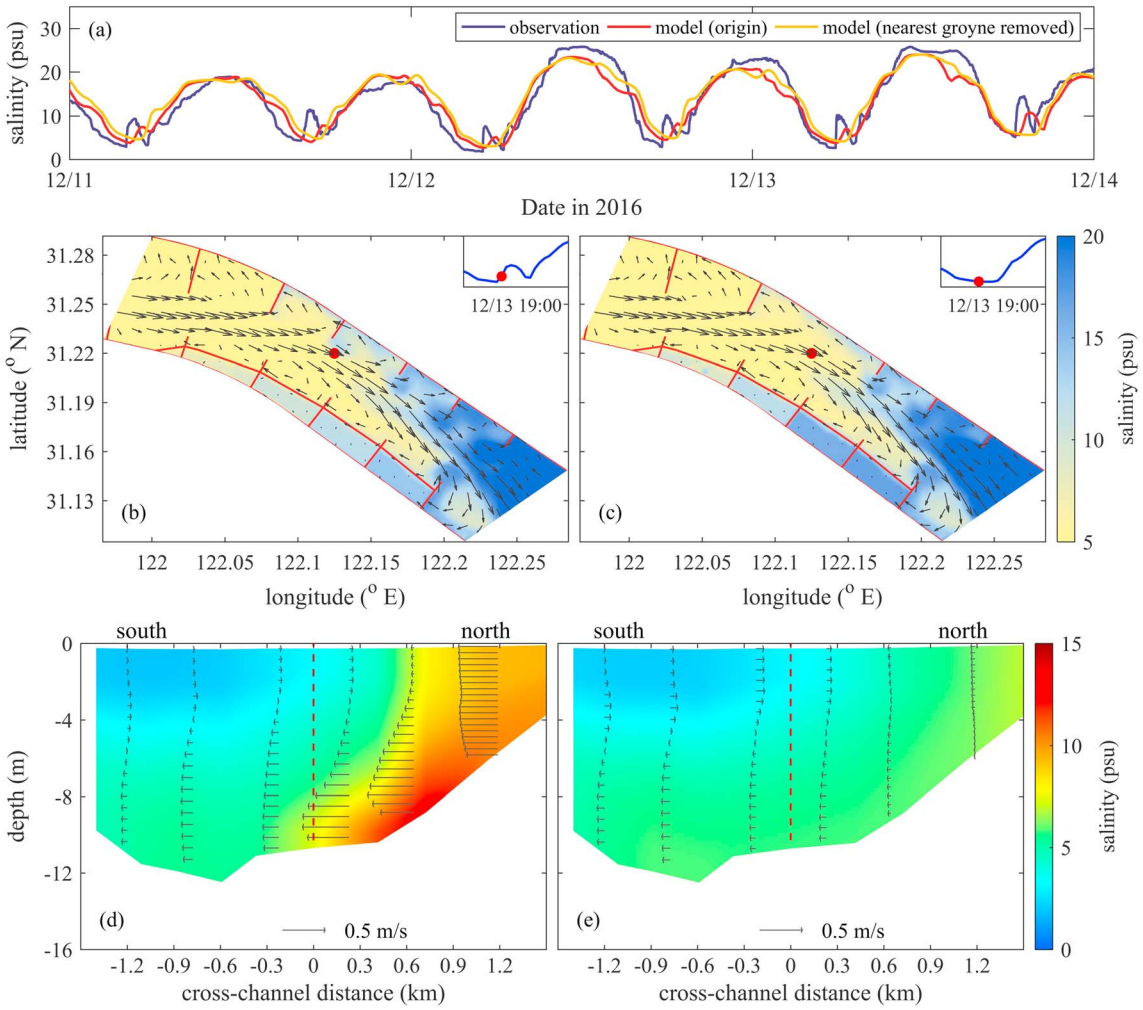

Figure 14. Model-data comparison with groyne-removed case added (a), comparison between original case (b, d), and groyne-removed case (c, e) at the same time in bottom salinity distribution (b, c) and vertical salinity distribution (d, e).

along-estuary dike (Figure 14b), which limited exchange flows between the groyne fields and the estuary. As a result, their salinity remained fairly constant in time (Figure 7) and cross-channel flows did not develop from the south (Figure 8).

The impact of groynes on lateral flows reported here has, to our knowledge, not been published elsewhere in the scientific literature but constitutes an important contribution. Many researchers have reported groynes' impacts on flow hydrodynamics (Brevis et al., 2014; McCoy et al., 2008; Sukhodolov, 2014) and mass exchange (McCoy et al., 2007; Uijttewaal et al., 2001; Weitbrecht et al., 2008). These studies do not include salinity-induced density effect, which is closely related to groynes. Groynes are used throughout the world to channelize flow, preventing siltation rates in fairways maintained to provide access to ships. Lateral flows may significantly contribute to near-bed sediment dynamics and siltation rates and therefore resulting in the exact opposite effect for which the groynes were originally designed. As a result, comprehensive understanding of the impact of such engineering works are required for sustainable development of human-impacted estuaries.

4.4. Implications of ISV in Other Studies

Earlier studies in the NP of the CE also identified the existence of ISV but were not paid much attention to. Song et al. (2013) conducted a quadrapod observation at the slightly south of the deep channel. They observed a similar ISV during the low water slack (in their Figure 2a). They used velocity skew and

flux skewness to examine the lateral sediment transport and identified a net sediment transport from the south groyne to the deep channel with an opposite lateral transport from the north to the south side of the channel in near-bottom area (below 1 mab). This opposite lateral flow and the ISV was likely generated with the same mechanisms discussed in our study. We believe that the ISV in their study was also generated by saline water trapped in the north groyne-sheltered area as this saline water mass could move across the deep channel to where Song et al. (2013) conducted the observation. Actually, the ISV in their study should be a further dispersion of ISV generated from the north shoal and that is why the magnitude of ISV at their observation site was much weaker. The lateral flow discussed in our study should be taken into account when considering sediment transport in the NP, as its movement affects the whole deep channel in the cross-channel direction. This will improve the knowledge of severe siltation issues in the channel.

ISV was also detected in other estuaries. Ralston et al. (2012) deployed fixed instruments frame in the channel and on the shoal of Hudson River estuary, which also revealed clear evidence for ISV (in their Figure 3a). The bottom salinity measured in the channel also varied within the tidal cycle during low water slack and was also the result of lateral flows. Their lateral flow was primarily related to topography features in a channel-shoal system. We believe that more estuaries and channels all over the world are characterized by lateral flows resulting in ISV's albeit that the responsible mechanism (in our case the BPG, in Ralston's case the topography) may differ.

The ISV directly gives a strong indication for lateral flows in a channel-shoal system. ISV can be a simple indicator of lateral flow and lateral processes, which should be considered when investigating the hydrodynamics and sediment dynamics of estuaries with extensive shoals. Actually, the ISV is just one typical feature under the modulation of lateral flow. Besides, particular small-scale fluctuation in other variables (for example, temperature) also occurs concurrently with ISV. Generally speaking, these small-scale fluctuations in multiple variables all indicate the importance of the lateral flow caused by many different reasons in a tidal channel-shoal system.

5. Conclusions

In this study, a tripod system integrated with multiple instruments was deployed in the NP of the CE to measure lateral flow and its impacted salinity transport. Observation results revealed periodic formation of ISV during low water slack. The tripod observations indicated that the ISV was generated by a near-bed lateral flow from the shallow shoal to the deep channel. A high-resolution unstructured-grid model for the CE has been applied to simulate this lateral flow and the salinity transport. The numerical simulation showed that the high-salinity water trapped over the shoal was transported to the deep channel during ebb tide. The momentum balance analysis based on model results identified that the density-induced BPG was the dominant physical mechanism for the generation of this lateral flow. Cross-channel residual current had a consistent near-bed shoal-to-channel component, which was closely connected with the shoal-to-channel lateral flow. Salinity transport also showed a southward net transport pattern.

This mechanism produced intratidal peaks in salinity and influenced pattern of stratification and mixing in the cross-channel section. Strong stratification occurred with and enhanced by the lateral flow, which can potentially affect sediment behavior (for example, hindered settling) and modulate the pattern of sediment transport.

The ISV can be a signal of active lateral process in a tidal estuary, especially in a human-impacted channel-shoal system. Our simulations show that dikes and groynes greatly influence the flow field in the channel and the retention effect of groynes predominantly contributes to this lateral flow. This conclusion reminds us of more caution when designing such engineering structures. The findings reported here provide a key element for future work on sedimentation issues, in general, but in the NP in particular, since our work suggests that groynes generate a residual current directed from the shoals to the channel.

In particular, the role of salinity-induced currents on sediment dynamics and sediment-induced density effect on lateral flows needs to be further investigated. Since the results reported in this study were observed and simulated under dry-season freshwater discharge from the upstream Changjiang, caution should be taken when applying these results to wet season when freshwater discharge can be 3 to 4 times larger. Additional observations and model simulations are needed in that case.

Acknowledgments

This work is supported by the National Key R&D Program of China (Grant 2016YFA0600903), the NSFC project (Grants 41776104 and 41761144062), the MOST project (Grants 2016YFE0133700 and 2017YFE0107400), and the KNAW project (Grant PSA-SA-E-02). All data sets used in this study are publicly available at https://figshare.com/s/d74327d26220f0802979.

References

Bowen, M. M. (2003). Salt transport and the time-dependent salt balance of a partially stratified estuary. *Journal of Geophysical Research*, *108*(C5), 3158. https://doi.org/10.1029/2001JC001231

Brevis, W., García-Villalba, M., & Niño, Y. (2014). Experimental and large eddy simulation study of the flow developed by a sequence of lateral obstacles. *Environmental Fluid Mechanics*, *14*(4), 873–893. https://doi.org/10.1007/s10652-013-9328-x

Chant, R. J. (2010). Estuarine secondary circulation. In A. Valle-Levinson (Ed.), *Contemporary issues in estuarine physics* (pp. 100–124). Cambridge: Cambridge University Press. https://doi.org/10.1017/CBO9780511676567.006

Chen, C., Beardsley, R., Cowles, G., Qi, J., Lai, Z., Gao, G., et al. (2013). An unstructured grid, Finite-Volume Coastal Ocean Model FVCOM —User manual. *Tech. Rep., SMAST/UMASSD-13-0701, Sch. for Mar. Sci. and Technol., Univ. of Mass. Dartmouth, New Bedford*., *C* (July), 416 pp. https://doi.org/10.1017/CBO9781107415324.004

Chen, C., Liu, H., & Beardsley, R. C. (2003). An unstructured grid, finite-volume, three-dimensional, primitive equations ocean model: Application to coastal ocean and estuaries. *Journal of Atmospheric and Oceanic Technology*, *20*(1), 159–186. https://doi.org/10.1175/1520-0426(2003)020<0159:AUGFVT>2.0.CO;2

Chen, W., & de Swart, H. E. (2018). Longitudinal variation in lateral trapping of fine sediment in tidal estuaries: Observations and a 3D exploratory model. *Ocean Dynamics*, *68*(3), 309–326. https://doi.org/10.1007/s10236-018-1134-z

Dube, A., Jayaraman, G., & Rani, R. (2010). Modelling the effects of variable salinity on the temporal distribution of plankton in shallow coastal lagoons. *Journal of Hydro-Environment Research*, *4*(3), 199–209. https://doi.org/10.1016/j.jher.2010.03.003

Dyer, K. R. (1986). *Coastal and estuarine sediment dynamics*. New York: John Wiley and Sons. Retrieved from https://books.google.nl/books?id=78kQAQAAIAAJ

Egbert, G. D., & Erofeeva, S. Y. (2002). Efficient inverse modeling of barotropic ocean tides. *Journal of Atmospheric and Oceanic Technology*, *19*(2), 183–204. https://doi.org/10.1175/1520-0426(2002)019<0183:EIMOBO>2.0.CO;2

Fischer, H. B. (1976). Mixing and dispersion in estuaries. *Annual Review of Fluid Mechanics*, *8*(1), 107–133. https://doi.org/10.1146/annurev.fl.08.010176.000543

Fugate, D. C., Friedrichs, C. T., & Sanford, L. P. (2007). Lateral dynamics and associated transport of sediment in the upper reaches of a partially mixed estuary, Chesapeake Bay, USA. *Continental Shelf Research*, *27*(5), 679–698. https://doi.org/10.1016/j.csr.2006.11.012

Galperin, B., Kantha, L. H., Hassid, S., & Rosati, A. (1988). A quasi-equilibrium turbulent energy model for geophysical flows. *Journal of the Atmospheric Sciences*, *45*(1), 55–62. https://doi.org/10.1175/1520-0469(1988)045<0055:AQETEM>2.0.CO;2

Ge, J., Chen, C., Qi, J., Ding, P., & Beardsley, R. C. (2012). A dike–groyne algorithm in a terrain-following coordinate ocean model (FVCOM): Development, validation and application. *Ocean Modelling*, *47*, 26–40. https://doi.org/10.1016/j.ocemod.2012.01.006

Ge, J., Ding, P., & Chen, C. (2014). Low-salinity plume detachment under non-uniform summer wind off the Changjiang Estuary. *Estuarine, Coastal and Shelf Science*, *156*(1), 61–70. https://doi.org/10.1016/j.ecss.2014.10.012

Ge, J., Ding, P., Chen, C., Hu, S., Fu, G., & Wu, L. (2013). An integrated East China Sea-Changjiang Estuary model system with aim at resolving multi-scale regional-shelf-estuarine dynamics. *Ocean Dynamics*, *63*(8), 881–900. https://doi.org/10.1007/s10236-013-0631-3

Ge, J., Shen, F., Guo, W., Chen, C., & Ding, P. (2015). Estimation of critical shear stress for erosion in the Changjiang Estuary: A synergy research of observation, GOCI sensing and modeling. *Journal of Geophysical Research: Oceans*, *120*, 8439–8465. https://doi.org/10.1002/2015JC010992

Ge, J., Zhou, Z., Yang, W., Ding, P., Chen, C., Wang, Z. B., & Gu, J. (2018). Formation of concentrated benthic suspension in a time-dependent salt wedge estuary. *Journal of Geophysical Research: Oceans*, *123*, 8581–8607. https://doi.org/10.1029/2018JC013876

Guo, W., Wang, X. H., Ding, P., Ge, J., & Song, D. (2018). A system shift in tidal choking due to the construction of Yangshan Harbour, Shanghai, China. *Estuarine, Coastal and Shelf Science*, *206*, 49–60. https://doi.org/10.1016/j.ecss.2017.03.017

Hoitink, A. J. F., van Maren, D. S., & Hoekstra, P. (2011). Mixing and stratification in a tropical tidal embayment subject to a distributed freshwater source. *Journal of Marine Systems*, *88*(1), 34–44. https://doi.org/10.1016/j.jmarsys.2011.02.015

Huijts, K. M. H., Schuttelaars, H. M., de Swart, H. E., & Valle-Levinson, A. (2006). Lateral entrapment of sediment in tidal estuaries: An idealized model study. *Journal of Geophysical Research*, *111*, C12016. https://doi.org/10.1029/2006JC003615

Kim, Y. H., & Voulgaris, G. (2008). Lateral circulation and suspended sediment transport in a curved estuarine channel: Winyah Bay, SC, USA. *Journal of Geophysical Research*, *113*, C09006. https://doi.org/10.1029/2007JC004509

Lacy, J. R., & Sherwood, C. R. (2004). Accuracy of a pulse-coherent acoustic Doppler profiler in a wave-dominated flow. *Journal of Atmospheric and Oceanic Technology*, *21*(9), 1448–1461. https://doi.org/10.1175/1520-0426(2004)021<1448:AOAPAD>2.0.CO;2

Lai, Z., Chen, C., Cowles, G. W., & Beardsley, R. C. (2010). A nonhydrostatic version of FVCOM: 1. Validation experiments. *Journal of Geophysical Research*, *115*, C11010. https://doi.org/10.1029/2009JC005525

Lerczak, J. A., & Rockwell Geyer, W. (2004). Modeling the lateral circulation in straight, stratified estuaries*. *Journal of Physical Oceanography*, *34*(6), 1410–1428. https://doi.org/10.1175/1520-0485(2004)034<1410:MTLCIS>2.0.CO;2

Lewis, R. (1997). *Dispersion in estuaries and coastal waters*. Hoboken, NJ: Wiley.

Liu, G., Zhu, J., Wang, Y., Wu, H., & Wu, J. (2011). Tripod measured residual currents and sediment flux: Impacts on the silting of the Deepwater Navigation Channel in the Changjiang Estuary. *Estuarine, Coastal and Shelf Science*, *93*(3), 192–201. https://doi.org/10.1016/j.ecss.2010.08.008

McCoy, A., Constantinescu, G., & Weber, L. (2007). A numerical investigation of coherent structures and mass exchange processes in channel flow with two lateral submerged groynes. *Water Resources Research*, *43*, W05445. https://doi.org/10.1029/2006WR005267

McCoy, A., Constantinescu, G., & Weber, L. J. (2008). Numerical investigation of flow hydrodynamics in a Channel with a series of groynes. *Journal of Hydraulic Engineering*, *134*(2), 157–172. https://doi.org/10.1061/(ASCE)0733-9429(2008)134:2(157)

Mellor, G. L., & Yamada, T. (1982). Development of a turbulence closure model for geophysical fluid problems. *Reviews of Geophysics*, *20*(4), 851. https://doi.org/10.1029/RG020i004p00851

Nidzieko, N. J., Hench, J. L., & Monismith, S. G. (2009). Lateral circulation in well-mixed and stratified estuarine flows with curvature. *Journal of Physical Oceanography*, *39*(4), 831–851. https://doi.org/10.1175/2008JPO4017.1

Postma, H. (1967). Sediment transport and sedimentation in the estuarine environment. In G. H. Lauff (Ed.), *Eustuaries* (Vol. 13, pp. 158–179). Washington DC: American Association for Advancement of Science. https://doi.org/10.4319/lo.1968.13.4.0725

Ralston, D. K., Geyer, W. R., & Warner, J. C. (2012). Bathymetric controls on sediment transport in the Hudson River estuary: Lateral asymmetry and frontal trapping. *Journal of Geophysical Research*, *117*, C10013. https://doi.org/10.1029/2012jc008124

Simpson, J. H., Brown, J., Matthews, J., & Allen, G. (1990). Tidal straining, density currents, and stirring in the control of estuarine stratification. *Estuaries*, *13*(2), 125. https://doi.org/10.2307/1351581

Song, D., Wang, X. H., Cao, Z., & Guan, W. (2013). Suspended sediment transport in the Deepwater Navigation Channel, Yangtze River Estuary, China, in the dry season 2009: 1. Observations over spring and neap tidal cycles. *Journal of Geophysical Research: Oceans*, *118*, 5555–5567. https://doi.org/10.1002/jgrc.20410

Sukhodolov, A. N. (2014). Hydrodynamics of groyne fields in a straight river reach: Insight from field experiments. *Journal of Hydraulic Research*, *52*(1), 105–120. https://doi.org/10.1080/00221686.2014.880859

Uijttewaal, W. S. J., Lehmann, D., & van Mazijk, A. (2001). Exchange processes between a river and its groyne fields: Model experiments. *Journal of Hydraulic Engineering*, *127*(11), 928–936. https://doi.org/10.1061/(ASCE)0733-9429(2001)127:11(928)

Wang, Z. B., van Maren, D. S., Ding, P. X., Yang, S. L., van Prooijen, B. C., De Vet, P. L. M., et al. (2015). Human impacts on morphodynamic thresholds in estuarine systems. *Continental Shelf Research*, *111*, 174–183. https://doi.org/10.1016/j.csr.2015.08.009

Weitbrecht, V., Socolofsky, S. A., & Jirka, G. H. (2008). Experiments on mass exchange between groin fields and main stream in rivers. *Journal of Hydraulic Engineering*, *134*(2), 173–183. https://doi.org/10.1061/(ASCE)0733-9429(2008)134:2(173)

Woodroffe, C. D., Nicholls, R. J., Saito, Y., Chen, Z., & Goodbred, S. L. (2006). Landscape variability and the response of Asian megadeltas to environmental change. In *Global change and integrated coastal management* (pp. 277–314). Dordrecht, The Netherlands: Springer.

Wu, J., Liu, J. T., & Wang, X. (2012). Sediment trapping of turbidity maxima in the Changjiang Estuary. *Marine Geology*, *303-306*, 14–25. https://doi.org/10.1016/j.margeo.2012.02.011

Zhu, L., He, Q., & Shen, J. (2018). Modeling lateral circulation and its influence on the along-channel flow in a branched estuary. *Ocean Dynamics*, *68*(2), 177–191. https://doi.org/10.1007/s10236-017-1114-8